Individualized cyclic mechanical loading improves callus properties during the remodelling phase of fracture healing in mice as assessed from time-lapsed *in vivo* imaging

Esther Wehrle[1], Graeme R Paul[1], Duncan C Tourolle né Betts[1], Gisela A Kuhn[1], Ralph Müller[1*]

[1] Institute for Biomechanics, ETH Zurich, Zurich, Switzerland.

Corresponding author:

Ralph Müller, PhD

Institute for Biomechanics

ETH Zurich

Leopold-Ruzicka-Weg 4

8093 Zurich, Switzerland

Email: ram@ethz.ch

Abstract

Fracture healing is regulated by mechanical loading. Understanding the underlying mechanisms during the different healing phases is required for targeted mechanical intervention therapies. Here, the influence of individualized cyclic mechanical loading on the remodelling phase of fracture healing was assessed in a mouse femur defect model. After bridging of the defect, a loading group (n=10) received individualized cyclic mechanical loading (8-16 N, 10 Hz, 5 min, 3x/week) based on computed strain distribution in the callus using animal-specific real-time micro-finite element analysis. Controls (n=10) received 0 N treatment at the same post-operative time-points. By registration of consecutive scans, structural and dynamic callus morphometric parameters were followed in three callus sub-volumes and the adjacent cortex showing that the remodelling phase of fracture healing is highly responsive to cyclic mechanical loading with changes in dynamic parameters leading to significantly larger callus formation and mineralization. Loading-mediated maintenance of callus remodelling was associated with distinct effects on Wnt-signalling-associated molecular targets Sclerostin and Rankl in callus sub-regions and the adjacent cortex. Given these distinct local protein expression patterns induced by cyclic mechanical loading, the femur defect loading model with individualized load application seems suitable to understand the local spatio-temporal mechano-molecular regulation of the different fracture healing phases.

Introduction

Mechanical loading is a key factor for normal progression of the fracture healing process. Delayed fracture repair and non-union formation is a major issue in orthopaedic surgery, with an incidence of 5-10% and a high socioeconomic burden [1,2] and has been partially attributed to low and inadequate mechanical loading of the defect region [3,4], affecting all consecutive phases (inflammation, repair, remodelling) of the fracture repair process. The local mechanical conditions in the fracture healing area (for details see tissue differentiation hypothesis by Claes & Heigele [5]) are crucial for the repair process by determining molecular and cellular reactions, the tissue to be formed and the type of ossification. We and others have previously shown that externally applied mechanical stimuli, either applied locally to the fracture site via dynamic fixators [6] or globally via whole body vibration platforms [7,8], can improve fracture healing. In contrast, inadequate mechanical stimuli resulting in a too low or too high interfragmentary motion were not successful or even impaired the healing process [9-11]; for review see [12]). In order to understand the underlying mechanisms, refined and well controlled *in vivo* loading models are needed. Recent studies particularly indicate that profound understanding of the local spatio-temporal mechanical regulation of the fracture healing process seems crucial for translation of this knowledge to the clinics, aiming at the development of safe, targeted and individualized mechanical intervention therapies. Whereas many preclinical fracture healing studies focused on improving the early healing phases (inflammation, repair) with the aim of increasing bone formation and achieving earlier bone union, recent studies also indicate a potential to improve fracture healing outcome via modulation of callus remodelling [13-15]. Given the strong influence of mechanical loading on normal bone remodelling, the application of controlled mechanical loading might

be suitable to also improve and accelerate the remodelling phase during fracture healing. However, preclinical fracture healing studies with application of loading have so far shown contradictory results [12] and have not been able to completely capture underlying mechanisms due to restrictions in study design: (I) cross-sectional setup with only end-point analyses, (II) effect assessment not specific to healing phases, (III) same load for all animals irrespective of individual callus properties and healing progression. We aim to overcome current limitations by combining state-of-the-art time-lapsed *in vivo* imaging with a novel precisely controlled femur defect loading system in mice. By applying time-lapsed *in vivo* micro-CT and animal-specific real-time micro-finite element analysis (micro-FEA), the developed femur defect loading model allows scaling of loading settings based on strain distribution in the callus [16], thereby considering individual differences in healing speed. To follow the healing progression in each animal, a recently developed longitudinal *in vivo* micro-CT based approach was applied, which was previously shown to capture the different healing phases and to discriminate physiological and impaired healing patterns [17], without significant radiation-associated effects on callus properties [18]. By registering consecutive scans of the defect region for each animal and implementing a two-threshold approach, data on bone turnover and mineralization kinetics can be obtained, which is particularly important for targeting callus remodelling under different conditions.

The objective of this study was to assess the influence of individualized cyclic mechanical loading on the remodelling phase of fracture healing via longitudinal *in vivo* micro-CT imaging. We hypothesized, that individualized cyclic mechanical loading improves structural and dynamic callus properties during the remodelling phase of fracture healing.

Results

By combining a novel *in vivo* femur defect loading model (Fig. 1 and Supplementary Fig. 1) with a recently established time-lapsed *in vivo* micro-CT based monitoring approach [18,19], the influence of individualized cyclic mechanical loading on callus properties was assessed during the remodelling phase of fracture healing. A loading group (n=10) received individualized cyclic mechanical loading (8-16 N, 10 Hz, 5 min, 3x/week) whereas controls (n=10) received 0N for 5 min at the same post-operative time-points. By registration of consecutive scans, structural and dynamic callus parameters were followed in three callus sub-volumes (defect centre: DC, defect periphery: DP, cortical fragment periphery: FP) and the adjacent cortical fragments (FC) over time (Fig. 2 and 3), for details on methods see Tourolle et al. 2019 [19]; for detailed study design see Supplementary Table S1).

General physical observation

All mice recovered rapidly from surgery. During the healing period, the animals' body weight did not significantly change compared to pre-operative values without significant differences between or within the two groups (see Supplementary Fig. S2). We also assessed the social interaction between mice (animals sitting in groups vs. separated from others) and the nesting behaviour (start of nest building after surgery). Specifically, all animals started to build nests on the day of surgery and were found in groups in the nest in the morning of post-operative day 1. Throughout the further healing period social interaction between mice and nesting behaviour did not differ from pre-surgical observations and was similar for animals of the scan and control groups.

110 **Volumes of interest (VOI) for evaluation by time-lapsed *in vivo* micro-CT**

111 In order to exclude bias in the further micro-CT analyses, we compared the size of the
112 different VOIs (depicted in Fig. 3; for details on VOI generation see Tourolle et al., 2020 [19]).
113 The VOIs encompassed the following volume for the control (n=10) and the loading group
114 (n=10): 1.14±0.13mm^3 vs. 1.04±0.16mm^3 for the defect centre (DC), 6.68±0.77mm^3 vs.
115 6.35±0.82mm^3 for the defect periphery (DP), 2.28±0.17mm^3 vs. 2.31±0.16mm^3 for the
116 cortical fragments (FC), 15.44±0.70mm^3 vs. 15.84±0.99mm^3 for the fragment periphery (FP).
117 No significant differences in volume were detected in any of the VOIs between groups.

118

119 **Pre-loading healing patterns monitored by time-lapsed *in vivo* micro-CT**

120 In the pre-loading healing period (week 0 to week 3) similar and physiological healing
121 patterns were observed for the control group (n=10) and the loading group (n=10) in all
122 defect VOIs (DC, DP and FP) and the adjacent cortex (FC; Fig. 2 and 3). Registration of
123 consecutive *in vivo* micro-CT scans allowed to capture distinct callus characteristics
124 indicative of the different healing phases (inflammation, repair, remodelling; significant
125 weekly differences in bone parameters indicated in Fig. 3). From week 0-1 to week 1-2 in
126 both groups a significant 4x to 14x increase in bone formation was detected in the three
127 callus VOIs DC (control group: p=0.0007; loading group: p=0.0006; Fig. 3a), DP (control
128 group: p<0.0001; loading group: p<0.0001; Fig. 3d) and FP (control group: p=0.0012; loading
129 group: p=0.0006; Fig. 3j), indicating progression from the inflammation to the reparative
130 phase. This led to a significant gain in bone volume (BV/TV) by week 2 in the callus VOIs DC
131 (control group: p<0.0001; loading group: p<0.0001; Fig. 3b), DP (control group: p<0.0001;
132 loading group: p<0.0001; Fig. 3e) and FP (control group: p<0.0001; loading group: p<0.0001;

133 Fig. 3k). From week 1-2 to week 2-3 a significant 3x to 9x increase in resorptive activities was
134 seen in the callus VOIs DC (control group: $p=0.0023$; loading group: $p<0.0001$; Fig. 3a), DP
135 (control group: $p=0.0499$; loading group: $p=0.0162$; Fig. 3d) and FP (control group: $p=0.0326$;
136 loading group: $p=0.0070$; Fig. 3j), indicating the progression from the repair to the
137 remodelling phase. From week 2 to week 3, the highly mineralized bone fraction in the callus
138 VOIs significantly increased ($p<0.0001$ in DC, DP, FP) in both groups, indicating callus
139 maturation (Fig. 3c, 3f and 3l).
140 From week 0 to week 3, in both groups, strong resorptive activities (Fig. 2 and 3g) were seen
141 in the adjacent cortical fragments (FC). BRR showed significantly weekly increases whereas
142 no significant weekly changes in bone formation were observed in this VOI. The strong
143 resorptive activities let to decreased bone volume by week 3 reaching statistical significance
144 in the loading group ($p<0.0001$). Furthermore, the fraction of highly mineralized bone
145 significantly decreased from week 1 to week 3 in both groups ($p<0.0001$), indicating cortical
146 reorganisation.
147
148 **Individualized cyclic mechanical loading improves callus properties during the remodelling**
149 **phase of fracture healing**
150 Individualized cyclic mechanical loading (8-16N, 10 Hz, 300 cycles, 3x/week) started after
151 bridging of the femur defect (week 3; Table 1) at the beginning of the remodelling phase
152 (loading group, n=10). RT-micro-FE allowed determination of initial loads (8-12N) based on
153 individual callus properties, weekly load-scaling (8-16N) and matching of strain distribution
154 in the callus for the 4-week loading period. Control animals received 0N loading at the same
155 post-operative time-points. Already after 1 week, the first loading-associated effects on

156 callus properties and the adjacent cortical bone were seen: Specifically, loading reduced BRR
157 in all VOIs in week 3-4 compared to pre-loading values in week 2-3 (Fig. 3a, d, g, j) reaching
158 statistical significance in DC ($p<0.0001$). In contrast, in the control group, BRR further
159 increased in all VOIS during the same period with statistical significance seen in the
160 peripheral VOIs ($p=0.0066$ for DP, $p=0.0126$ for FP). From week 3-4 to week 6-7, the applied
161 individualized mechanical loading was also able to maintain bone formation at significantly
162 higher levels compared to controls, while bone resorption was significantly reduced during
163 the same period. This led to a linear increase in osseous callus volume in loaded animals
164 from week 3 to week 7 in all callus VOIs (DC: +41 %, DP: +130 %, FP: +111 %) and the
165 adjacent cortex (FC: +20 %), whereas it significantly declined in controls (DC: - 28 %, DP: - 44
166 %, FP: -27 %, FC: -30 %). In week 6-7, no significant differences in bone turnover were seen
167 anymore indicating load adaptation. After 7 weeks, loaded animals had significantly more
168 bone in the defect (2x for DC, $p<0.0001$; 4x for DP, $p<0.0001$; 3x for FP, $p<0.0001$) with a
169 significantly larger fraction of highly mineralized bone compared to controls (+8% for DC,
170 $p=0.0006$; +15% for DP, $p<0.0015$; +10% for FP, $p<0.0001$). Three-point bending also showed
171 a 46% higher relative bending stiffness (healed femur vs. contralateral femur) in the loaded
172 animals (107%) compared to controls (73%; n=2/group). In addition, according to the
173 standard clinical evaluation of X-rays, the number of bridged cortices per callus was
174 evaluated in two perpendicular planes and animals with ≥3 bridged cortices were
175 categorized as healed. From week 4 to week 7 all defects in both groups were categorized as
176 healed (Table 1), indicating that the applied forces during cyclic mechanical loading did not
177 lead to re-fracture of the callus.

178 Loading also affected the bone turnover in the adjacent cortex (FC). Already after 1 week,
179 loaded animals showed significantly lower cortical bone resorption compared to controls
180 (Fig. 3 j). Whereas cortical volume significantly declined ($p<0.0001$) in control animals from
181 week 3 to week 7 by 27%, it significantly increased ($p<0.0001$) by 20% in the loaded animals
182 during the same time period (Fig. 3k). From week 4 to week 7 loading was also associated
183 with significantly higher cortical mineralization (+4% in week 4 to +54% in week 7) compared
184 to controls (week 4: $p=0.0459$, week 5 – week 7: $p<0.0001$; Fig. 3l)).
185 In week 7, the FC VOI comprised 46% and 34% of the osseous tissue in the total VOI (TOT)
186 for the control and loading group, respectively. In the DC VOI, 20% (control group) and 17%
187 (loading group) of the total bone volume were seen. In the two peripheral VOIs, 9% (control
188 group) and 14% (loading group) of the total osseous tissue were seen in the DP and 26%
189 (control group) and 35% (loading group) in the FP VOI. Loading was associated with a shift in
190 the bone distribution from the cortical fragments to the peripheral VOIs.
191 *Ex vivo*, 3-point-bending testing was performed on healed femora and contralateral femora
192 of two animals from the loading and the control group. The relative bending stiffness (healed
193 femur vs. contralateral femur) was 107% in the loading group and 73% in the control group,
194 indicating loading-associated improved functional healing outcome.
195
196 **Histology**
197 In order to also visualize the tissue composition of the callus, we performed end point
198 histological stainings of serial sections from one animal of each group. Histology supported
199 our micro-CT findings with complete cortical bridging seen in the animal from the loading
200 and from the control group (Fig. 4 B-I). However, the loaded animal showed a larger callus

201 with some cartilage fractions suggesting ongoing endochondral ossification processes,
202 whereas in the control animal the callus was largely remodelled with restoration of the
203 medullary cavity indicating proceeding towards the end of healing (Fig. 4 b-e). Furthermore,
204 differences in the shape of the cell nuclei were observed between the osteocytes in the
205 fracture callus (round shape) of the loaded animal in comparison to the cell nuclei seen in
206 the cortical bone of the same animal (ellipsoidal shape) and the cell morphology seen in the
207 control animals (Fig. 5 a+b), suggesting an association between the local mechanical
208 environment and cellular morphology. In regions with lower strains visualized by micro-FE
209 (endosteal fracture callus; Fig. 4a and 5b), rounder cell nuclei were observed, compared to
210 ellipsoidal nuclei shape in higher strained regions (cortex; Fig. 4a and 5b). To capture
211 potential underlying mechano-molecular targets, we performed immunohistochemistry of
212 Sclerostin (inhibitor of the mechano-responsive and osteoanabolic Wnt signalling pathway)
213 and Rankl (negatively-regulated target gene of Wnt signalling) which have both previously
214 been associated with the mechanical regulation of bone adaptation and healing [8,20-24].
215 Sclerostin staining seemed less abundant in the fracture callus compared to the cortical bone
216 of the loaded animal (Fig. 4 f and 5b) with no region-specific differences in staining patterns
217 being seen in the control animal (Fig. 4g and Fig. 5b), suggesting that Wnt-signalling
218 contributes to the loading-mediated osteoanabolic effects on fracture healing seen in this
219 study. Surprisingly, at the same time Rankl, which is down-regulated by Wnt-signalling, was
220 more abundantly and stronger expressed in the callus of the loaded animal compared to the
221 control animal (Fig. 4 h+i and Fig. 5b), indicating that not only Wnt-signalling, but also other
222 molecular factors and signalling pathways have to be involved in the observed mechanically-
223 mediated effects on callus properties during the remodelling phase of fracture healing. In

224 line with previous studies, strong Rankl expression was seen in lowly strained callus regions
225 as visualized via micro-FE analysis (Fig. 4a and 5b), indicating ongoing bone remodelling.
226
227 **Discussion**
228 In this study, the effect of individualized cyclic mechanical loading on the remodelling phase
229 of fracture healing was assessed in a novel femur defect loading model in mice using a
230 recently developed *in vivo* micro-CT based monitoring approach. Given the strong mechano-
231 responsiveness of bone cells, several studies have applied mechanical loading (e.g. globally
232 via vibration platforms, or locally via external fixators) to improve fracture healing showing
233 contradictory results. Whereas some studies saw a loading-mediated improvement of
234 fracture healing, others were not successful or even reported an impairment of the fracture
235 healing process [9-11]. One limitation of these studies was the application of the same load to
236 all animals irrespective of individual differences in healing progression, which bears the risk
237 of re-fracturing lowly mineralized bone after initial bridging of the defect. In order to allow
238 for individualized mechanical loading we now developed a precisely controlled *in vivo*
239 loading model based on external fixation of femur defects in mice. By combining state-of-
240 the-art time-lapsed *in vivo* imaging with individualized mechanical loading protocols adapted
241 to animal-specific callus properties, this allows to precisely characterize spatio-temporal
242 effects of mechanical loading on the fracture callus. Given the high mechano-responsiveness
243 of bone cells during normal bone remodelling and as recent studies also indicate a potential
244 to improve fracture healing outcome via modulation of callus remodelling [13-15], we focused
245 this study on the effect of mechanical loading on callus properties during the remodelling
246 phase of fracture healing.

247 Via weekly *in vivo* micro-CT imaging, we saw, that cyclic mechanical loading linearly
248 increased the osseous callus volume during the remodelling phase of fracture healing, so
249 that by the study end, loaded animals had significantly more bone in all callus VOIs (2x for
250 DC, $p<0.0001$; 4x for DP, $p<0.0001$; 3x for FP, $p<0.0001$) with a significantly larger fraction of
251 highly mineralized bone compared to controls (+8% for DC, $p=0.0006$; +15% for DP,
252 $p<0.0015$; +10% for FP, $p<0.0001$). This is supported by a recent study from Liu et al. [25]
253 describing additional loading-mediated bone formation during the remodelling phase in a
254 uni-cortical tibia defect model in mice. However, they failed to show statistical significance
255 between the loading and the control group in histomorphometry and micro-CT analyses,
256 which they attributed to the high variability within groups. As the study applied the same
257 load to all animals irrespective of healing progression, differences in the induced strains
258 might have caused the high variability within groups. We addressed this by using our
259 recently developed real-time micro-FE based loading approach [16], which takes into account
260 the individual strain distribution within the callus for determining individual loading settings
261 at weekly post-operative intervals. So far, no study using a complete defect model assessed
262 the effect of local cyclic mechanical loading (e.g. via external fixators, tibia/ulna-loading)
263 when exclusively applied during the remodelling phase of the healing process. An earlier
264 tibia defect loading study (defect size: 3 mm) in sheep by Goodship et al. [6] applied cyclic
265 mechanical loading (25 µm interfragmentary movement, 30 Hz) throughout the healing
266 period (week 0 - week 10, 5x per week) and reported a significantly larger callus with higher
267 mineralization in loaded animals compared to controls. However, as the loading application
268 was not restricted to specific post-operative time frames, it was not possible to evaluate
269 whether loading during a specific fracture healing period was sufficient for the observed

270 improvement in fracture healing or if cyclic mechanical loading needs to be applied
271 throughout the healing process to achieve such an effect. We now showed, that the
272 remodelling phase is highly responsive to cyclic mechanical loading applied after initial
273 cortical bridging of the defect, with pronounced effects on callus size and mineralization. Via
274 limiting the loading application to the earlier healing period (day 7 – day 19), Gupta et al. [26]
275 aimed at assessing (histomorphometry and radiography on day 42) whether there is a
276 sustained effect of cyclic mechanical loading (2%, 10% and 30% strain, 0.5 Hz, 500 cycles) on
277 fracture healing outcome. They found a larger bone fraction in the callus and higher cortical
278 bridging scores in the loaded compared to the control animals, indicating, that loading
279 effects persisted after a 4-week non-loading period. In contrast to these studies, Schwarz et
280 al. [27] did not observe any loading-mediated improvement on fracture healing in a critically-
281 sized femur defect model in rats (defect size: 5mm). However, in this study loading (6 cycles
282 of constant loading at 500 µm IFM and 40s rest phase), was only applied once per week,
283 which indicates a critical role of the type of loading (constant vs. cyclic) and the frequency of
284 loading sessions per week. Whether cyclic mechanical loading in contrast to constant
285 mechanical loading is able to prevent non-union formation in critically-sized defects needs to
286 be assessed in future studies.
287 Via registration of longitudinal *in vivo* micro-CT scans (for details see Tourolle et al. 2019 [19]),
288 we were now for the first time able to also include dynamic parameters such as bone
289 formation and resorption in the monitoring of loading-mediated effects on fracture healing.
290 Compared to histology-based determination of the bone formation rate via *in vivo*
291 application of fluorescent dyes (e.g. calcein, alizarin), our micro-CT-based monitoring
292 approach with registration of consecutive scans also allows for assessment of the bone

resorption rate in individual animals, which was shown to be particularly suited for the characterization of the remodelling phase during the fracture healing process [17,18]. The most striking loading-mediated effect in the current study was the prompt and significant reduction in bone resorption rate (week 3-4 vs. week 2-3), which was seen in the central and periosteal VOIs (DC, FP) as early as 1 week after loading (Fig. 3A, 3J). Compared to control animals, in which bone resorption still increased during this early remodelling period (week 3-4), loaded animals showed significantly lower bone resorption rates in all callus VOIs (DC, DP, FP) in this first week of loading, indicating a strong mechano-responsiveness of the fracture callus during this healing period. Most of the previous studies either assessed the loading effects only after a longer loading period of minimum 2 weeks [27,28] or they did not see significant loading-mediated effects on the fracture callus after shorter treatment periods [8,10,26]. So far only one study by Leung et al. [29] was able to detect a loading-mediated improvement of fracture healing (larger callus diameter) after a short loading period of 1 week. We were now able to strengthen these cross-sectional structural callus findings with our longitudinal micro-CT data obtained for single animals. In respect to the underlying mechanisms, we showed for the first time, that not only bone formation but also bone resorption can be significantly modulated via cyclic mechanical loading during fracture healing, indicating a potential for mechanical intervention therapies to improve impaired fracture healing conditions associated with imbalanced bone remodelling. Furthermore, implementation of our two-threshold approach showed cyclic mechanical loading to be also effective in significantly advancing callus mineralization compared to control animals. Via combining our novel loading model with time-lapsed *in vivo* imaging and a two-threshold approach, we were able to characterize the spatio-temporal effects of loading during the

316 remodelling phase of fracture healing. Furthermore, the applied micro-FE-based loading
317 approach also allowed for spatio-temporal visualization of strains induced in the fracture
318 callus (Fig. 4a+b). In order to also visualize the tissue composition of the callus, we
319 performed end point histological stainings of serial sections from one animal of each group.
320 Histology supported our micro-CT findings with complete cortical bridging seen in both
321 groups. However, the loaded animal showed a larger callus with some cartilage fractions
322 suggesting ongoing endochondral ossification processes, whereas in the control animal the
323 callus was largely remodelled with restoration of the medullary cavity indicating proceeding
324 towards the end of healing. Furthermore, differences in the shape of the cell nuclei were
325 seen between the osteocytes in the fracture callus (round shape) of the loaded animal in
326 comparison to the cell nuclei seen in the cortical bone of the same animal (ellipsoidal shape)
327 and the cell morphology seen in the control animals. This is particularly interesting, as
328 previous *in vitro* studies found, that round cells are more sensitive to mechanical loading
329 compared to flat and elongated cells [30-32], suggesting that repeated cyclic mechanical loading
330 might be able to induce round cellular morphology of (early) osteocytes, thereby
331 maintaining the remodelling phase of fracture healing eventually leading to higher
332 mineralization of the newly formed tissue compared to controls. To capture potential
333 underlying molecular targets, we performed immunohistochemistry of Sclerostin (inhibitor
334 of the mechano-responsive and osteoanabolic Wnt signalling pathway) and Rankl
335 (negatively-regulated target gene of Wnt signalling) which have both previously been
336 associated with the mechanical regulation of bone adaptation and healing [8,20-24]. Whereas
337 Sclerostin staining seemed less abundant in the fracture callus compared to the cortical bone
338 of the loaded animal (Fig. 4f, Fig. 5b), no region-specific differences in staining patterns were

339 seen in the control animal (Fig. 4g, Fig. 5b). This might indicate that Wnt-signalling
340 contributes to the loading-mediated osteoanabolic effects on fracture healing seen in this
341 study. However, at the same time we saw more and stronger Rankl staining in the callus of
342 the loaded animal compared to the control animal (Fig. 4 h+i). This finding precludes that the
343 loading-mediated increases in Rankl expression seen in this study were solely mediated via
344 Wnt-signalling but rather an interplay with further signalling pathways must have triggered
345 this strong response in Rankl production. Via micro-FE analysis, we saw high Rankl
346 expression in the lowly strained endosteal fracture callus, indicating ongoing bone
347 remodelling. In order to shed light into the complex interplay between a multitude of
348 mechano-responsive molecules and signalling pathway, novel advents in RNAsequencing
349 including spatial transcriptomic approaches might, in future studies, open interesting
350 possibilities to understand the spatio-temporal mechanomics of fracture healing. In non-
351 fractured bone, some of these molecular technologies (e.g. microarrays, [33-35]) have already
352 been successfully applied to study mechano-molecular effects in well-controlled and
353 characterized loading models (e.g. ulna, tibia and tail loading) in rodents. Targets (e.g.
354 Sclerostin, Estrogen signalling) found via these comprehensive studies were then assessed in
355 detail in further studies using either models with local [36-38] or global load application [39]. As
356 the main underlying mechanisms of bone adaptation to loading were identified using local
357 models of loading (ulna, tibia ..), this indicates that comprehensive spatio-temporal
358 mechano-molecular analyses in fracture healing will require tightly regulated models with
359 local application of mechanical loading being more controllable and less prone to variation
360 induced by confounding factors compared to models with global loading application.

361 In summary, using our recently developed femur defect loading model in combination with
362 time-lapsed *in vivo* micro-CT and a two-threshold approach, we showed that the remodelling
363 phase of fracture healing is highly responsive to cyclic mechanical loading with changes in
364 dynamic callus parameters leading to larger callus formation and mineralization. Loading-
365 mediated maintenance of callus remodelling was associated with distinct effects on the Wnt-
366 signalling-associated molecular targets Sclerostin and Rankl in callus sub-regions and the
367 adjacent cortex as assessed via immunohistochemistry. Given these distinct local protein
368 expression patterns induced by external cyclic mechanical loading, our tightly-controlled
369 femur defect loading model with individualized load application could be used in future
370 studies to precisely understand the local spatio-temporal mechano-molecular regulation of
371 the different fracture healing phases. With our real-time micro-FE based approach for
372 individualized load application considering differences in defect geometry and healing
373 progression, the femur defect loading model could also be used to study the bone
374 regeneration capacity of biomaterials under load application. With further advents in
375 transcriptomics and registration techniques for different imaging technologies, the tightly
376 controlled femur defect loading model could widen our knowledge on the spatio-temporal
377 regulation fracture mechanomics relevant for application of mechanical intervention
378 therapies to clinical settings for improvement of impaired healing conditions.
379

380 **Methods**

381 **Study design**

382 By combining a novel *in vivo* femur defect loading model with a recently established time-
383 lapsed *in vivo* micro-CT based monitoring approach, the influence of individualized cyclic

384 mechanical loading on callus properties was assessed during the remodelling phase of
385 fracture healing. All mice received a femur defect and post-operative micro-CT scans (vivaCT
386 40, ScancoMedical, Brüttisellen, Switzerland) were performed. After bridging of the femur
387 defect (week 3), real-time micro-FE allowed determination of initial loads (8N-12N), and
388 weekly load-scaling and matching of strain distribution in the callus for the 4 week loading
389 period. The loading group (n=10) received individualized cyclic mechanical loading (8-16N,
390 10 Hz, 5 min, 3x/week) whereas controls (n=10) received 0N for 5 min at the same post-
391 operative time-points. By registration of consecutive scans, structural and dynamic callus
392 parameters were followed in three callus sub-volumes (defect centre: DC, defect periphery:
393 DP, cortical fragment periphery: FP) and the adjacent cortical fragments (FC) over time
394 (Figure 1, for details on methods see Tourolle et al. 2020[19]; for detailed study design see
395 Supplementary Fig. S1).
396
397 **Animals**
398 All animal procedures were approved by the authorities (licence number: 36/2014;
399 Kantonales Veterinäramt Zürich, Zurich, Switzerland). We confirm that all methods were
400 carried out and reported in accordance with relevant guidelines and regulations (Swiss
401 Animal Welfare Act and Ordinance (TSchG, TSchV) and ARRIVE guidelines). To study adult
402 fracture healing female 12 week-old C57BL/6J mice were purchased from Janvier (Saint
403 Berthevin Cedex, France) and housed in the animal facility of the ETH Phenomics Center
404 (EPIC; 12h:12h light-dark cycle, maintenance feed (3437, KLIBA NAFAG, Kaiseraugst,
405 Switzerland), 5 animals/cage) for 8 weeks. At an age of 20 weeks, all animals received a
406 femur defect by performing an osteotomy with a 0.66mm Gigli wire saw as previously

407 described (group 1: control group, n=10; group 2: loading group, n=10; housing after
408 surgery: 2-3 animals/cage; for details on study design see Supplementary Table 1). All defect
409 surgeries were performed by the same veterinarian. Perioperative analgesia (25 mg/L,
410 Tramal®, Gruenenthal GmbH, Aachen, Germany) was provided via the drinking water two
411 days before surgery until the third post-operative day. For surgery and micro-CT scans,
412 animals were anaesthetized with isoflurane (induction/maintenance: 5%/1-2%
413 isoflurane/oxygen). Perioperative handling, and monitoring, micro-CT imaging and loading
414 application was performed by the surgeon.
415
416 **Loading fixator assembly and group assignment**
417 The four parts of the loading fixators (n=20) were assembled as depicted in Suppl. Fig. 1. To
418 allow optimal identification throughout the experiments, one side part was engraved with a
419 fixator-specific number (Suppl. Fig 1A, 1B). The stiffness of each fixator was measured using
420 a Zwick testing machine and the fixators were assigned to the two groups, to allow similar
421 distributions of fixator stiffness in the loading and control group (Suppl. Fig 1C).
422
423 **Femur osteotomy**
424 In all animals an external fixator (Mouse ExFix, RISystem, Davos, Switzerland; mean stiffness:
425 17N/mm; Suppl. Fig. 1) was positioned at the craniolateral aspect of the right femur and
426 attached using four mounting pins. First, the most proximal pin was inserted approximately
427 2mm proximal to the trochanter, followed by placement of the most distal and the inner
428 pins. Subsequently, a femur defect was created using a Gigli wire (diameter: 0.66mm).
429

430 **Time-lapsed *in vivo* micro-CT**

431 Immediate post-surgery correct positioning of the fixator and the defect was visualized using
432 a vivaCT 40 (Scanco Medical AG, Brüttisellen, Switzerland) (isotropic nominal resolution: 10.5
433 µm; 2 stacks of 211 slices; 55 kVp, 145 µA, 350 ms integration time, 500 projections per
434 180°, 21 mm field of view (FOV), scan duration ca. 15 min). Subsequently, the fracture callus
435 and the adjacent bone between the inner pins of the fixator were scanned weekly using the
436 same settings. Scans were registered consecutively using a branching scheme (registration of
437 whole scan for bridged defects; separate registration of the two fragments for unbridged
438 defects)[5]. Subsequently, morphometric indices (bone volume - BV, bone volume/total
439 volume – BV/TV, bone formation rate – BFR, bone resorption rate - BRR) were computed
440 (threshold: 395mg HA/cm^3; for details on methods see Tourolle et al., 2020 [19]). To assess
441 mineralization progression, a second threshold (645mg HA/cm^3) was applied and the ratio
442 between highly and lowly mineralized tissue (BV_{645}/BV_{395}) was calculated. The two selected
443 thresholds are included in our recently developed multidensity threshold approach [19].
444 According to the standard clinical evaluation of X-rays, the number of bridged cortices per
445 callus was evaluated in two perpendicular planes (UCT Evaluation V6.5-1, Scanco Medical
446 AG, Brüttisellen, Switzerland). A ‘‘healed fracture’’ was considered as having a minimum of
447 at least three bridged cortices per callus.

448 For evaluation, four volumes of interest (VOIs) were defined, which were created
449 automatically from the post-operative measurement (Fig. 1): defect centre (DC), defect
450 periphery (DP), cortical fragment centre (FC), and fragment periphery (FP). Data were
451 normalised to the central VOIs: DC/DC, DP/DC, FC/FC, FP/FC.

452

453 **Individualized cyclic mechanical loading**

454 From week 4 to week 7, individualized cyclic loading (8-16N, 10Hz, 3000cycles; 3x/week;
455 controls - 0N) was applied via the external loading fixator (Suppl. Fig 1B) based on computed
456 strain distribution in the callus using animal-specific real-time micro-finite element (RT-
457 microFE) analysis (for detailed description of methods see [16]. Briefly, after weekly micro-CT
458 measurements of each animal, the images were pre-processed using threshold-binning to
459 create a high-resolution multi-density FE mesh, which was then solved on a supercomputer
460 within the same anaesthetic session for each mouse. 2D and 3D visualizations of the callus
461 were generated and a strain histogram was plotted. This information allowed load scaling
462 based on the strains induced in the callus in individualized animals. Specifically, the
463 distribution was scaled to achieve a median effective microstrain of 700. To assess regions
464 that posed a failure risk the 99th percentile strains of each simulation was visualised in both
465 image based and histogram forms. If more than 50 voxels exceeded 1% then the optimised
466 load was reduced by 1 N.

467

468 **Mechanical testing**

469 3 point bending tests were performed on a Zwick compression tester (ZwickRoell GmbH &
470 Co, Ulm, Germany). Tests were conducted on a setup of 8 mm support span and up to 3 N.
471 Tests were performed quasi-statically with a cross-head speed of 0.4 mm/min. Stiffness was
472 then calculated from the linear region of the resultant force-displacement curve. Each
473 sample was tested three times and the mean stiffness was taken.

474

475

476 **Histology**

477 Histological stainings were performed in one animal per group. On day 49, femora were
478 excised, the femoral head was removed and the samples were placed in 4% neutrally
479 buffered formalin for 24 hours and subsequently decalcified in 12.5% EDTA for 10-14 days.
480 The samples were embedded in paraffin and the complete fracture callus was cut in 10 µm
481 longitudinal serial sections. Every 10th section was stained with Safranin-O: Weigert's iron
482 haematoxylin solution (HT1079, Sigma-Aldrich, St. Louis, MO) - 4min, 1:10 HCl-acidified 70%
483 ethanol - 10s, tap water - 5min, 0.02% Fast Green (F7258, Sigma-Aldrich, St. Louis, MO) -
484 3min, 1% acetic acid - 10s, 0.1% Safranin-O (84120, Fluka, St. Louis, MO) - 5min. Images
485 were taken with Slide Scanner Pannoramic 250 (3D Histech, Budapest, Hungary) at 20x
486 magnification. Sections in between were stained for Sclerostin and Rankl.

487 For immunohistochemical staining of Sclerostin, nonspecific sites were blocked (1% BSA/PBS
488 + 1% rabbit serum) for 60 min at room temperature. Subsequently, the sections were
489 incubated with the primary antibody against Sclerostin (AF1589, R&D Systems, Minneapolis,
490 MN; 1:150 in 1%BSA/PBS + 0.2% rabbit serum) overnight at 4°C. To detect the primary
491 antibody, a secondary biotinylated rabbit anti-goat-IgG antibody (BAF017, R&D Systems,
492 Minneapolis, MN) was added for 1 h at room temperature. For signal amplification, the
493 slides were incubated with avidin-biotin complex (PK-6100 Vector Laboratories, Burlingame,
494 CA) for 30 min. Diaminobenzidine (Metal Enhanced DAB Substrate Kit, 34065 ThermoFisher
495 Scientific, Waltham, MA) was used as detection substrate. Counterstaining was performed
496 with FastGreen (F7258, Sigma-Aldrich, St. Louis, MO).

497 For immunohistochemical staining of Rankl, slides were placed into TBS-Tween buffer and
498 inserted into the Dako-Autostainer (Dako, Ft. Collins, USA) using the following staining

499 protocol: incubation with primary antibody against Rankl (1:100; ab 9957, Abcam,
500 Cambridge, UK) at 4°C overnight, rinsing with TBS-Tween, peroxidase blocking for 10min at
501 room temperature, rinsing with TBS-Tween, Envision+System HPR Rabbit (Dako K4003) for
502 60 min at room temperature, rinsing with TBS-Tween and incubation with DAB (Dako
503 K3468) for 10 min at room temperature. The slides were rinsed in A. dest and
504 counterstained with FastGreen for 2sec.
505 For both immunohistochemical stainings, species-specific IgG was used as isotype control.
506 Images were taken with Slide Scanner Pannoramic 250 (3D Histech, Budapest, Hungary) at
507 40x magnification.
508
509 **Statistics**
510 Data were tested for normal distribution (Shapiro-Wilk-Test) and homogeneity of variance
511 (Levene-Test). Depending on the test outcome, group comparisons (loading vs. control
512 group) of data derived at single time points (VOI size) were performed by two-tailed
513 Student's t-test or Mann-Whitney U-test (IBM SPSS Statistics Version 23). For statistical
514 evaluation of repeated measurements two-way ANOVA with Geisser-Greenhouse correction
515 and Bonferroni correction (GraphPad Prism 8) were performed. The level of significance was
516 set at $p < 0.05$.
517
518 **Acknowledgements**
519 We thank Marco Hitz, Peter Schwilch, Angad Malhotra and Jianhua Zhang for technical and
520 surgery assistance. We thank Christopher M. O'Neill for the micro-CT and micro-FE images
521 depicted in Figure 4. The authors gratefully acknowledge support from the EU (BIODESIGN

522 FP7-NMP-2012-262948 and ERC Advanced MechAGE ERC-2016-ADG-741883). E. Wehrle
523 received funding from the ETH Postdoctoral Fellowship Program (MSCA-COFUND, FEL-
524 25_15-1).

525

526 **Author Contributions Statement**

527 The study was designed by E.W., G.A.K., and R.M.. The experiments were performed by
528 E.W. and G.R.P. Data analyses were performed by E.W., G.R.P. and D.C.B.. The manuscript
529 was written by E.W. and reviewed and approved by all authors.

530

531 **Data availability**

532 All necessary data generated or analysed during the present study are included in this
533 published article and its Supplementary Information files (preprint available on BioRxiv
534 (BIORXIV/). Additional information related to this paper may be requested from the authors.

535

536 **Competing Interests**

537 The authors declare no competing interests.

538

539 **References**

540 1 Einhorn, T. A. & Gerstenfeld, L. C. Fracture healing: mechanisms and interventions. *Nat Rev*
541 *Rheumatol* **11**, 45-54, doi:10.1038/nrrheum.2014.164 (2015).
542 2 Gomez-Barrena, E. *et al.* Bone fracture healing: Cell therapy in delayed unions and
543 nonunions. *Bone* **70**, 93-101, doi:10.1016/j.bone.2014.07.033 (2015).
544 3 Bottlang, M. *et al.* Effects of Construct Stiffness on Healing of Fractures Stabilized with
545 Locking Plates. *J Bone Joint Surg Am* **92a**, 12-22, doi:10.2106/Jbjs.J.00780 (2010).
546 4 Steiner, M., Claes, L., Ignatius, A., Simon, U. & Wehner, T. Numerical Simulation of Callus
547 Healing for Optimization of Fracture Fixation Stiffness. *Plos One* **9**, doi:ARTN
548 e10137010.1371/journal.pone.0101370 (2014).

5 Claes, L. E. & Heigele, C. A. Magnitudes of local stress and strain along bony surfaces predict the course and type of fracture healing. *J Biomech* **32**, 255-266, doi:Doi 10.1016/S0021-9290(98)00153-5 (1999).

6 Goodship, A. E., Lawes, T. J. & Rubin, C. T. Low-Magnitude High-Frequency Mechanical Signals Accelerate and Augment Endochondral Bone Repair: Preliminary Evidence of Efficacy. *J Orthop Res* **27**, 922-930, doi:10.1002/jor.20824 (2009).

7 Shi, H. F., Cheung, W. H., Qin, L., Leung, A. H. C. & Leung, K. S. Low-magnitude high-frequency vibration treatment augments fracture healing in ovariectomy-induced osteoporotic bone. *Bone* **46**, 1299-1305, doi:10.1016/j.bone.2009.11.028 (2010).

8 Wehrle, E. *et al.* The impact of low-magnitude high-frequency vibration on fracture healing is profoundly influenced by the oestrogen status in mice. *Dis Model Mech* **8**, 93-104, doi:10.1242/dmm.018622 (2015).

9 Stuermer, E. K. *et al.* Musculoskeletal Response to Whole-Body Vibration During Fracture Healing in Intact and Ovariectomized Rats. *Calcified Tissue Int* **87**, 168-180, doi:10.1007/s00223-010-9381-0 (2010).

10 Wehrle, E. *et al.* Distinct Frequency Dependent Effects of Whole-Body Vibration on Non-Fractured Bone and Fracture Healing in Mice. *J Orthop Res* **32**, 1006-1013, doi:10.1002/jor.22629 (2014).

11 Wolf, S. *et al.* Effects of high-frequency, low-magnitude mechanical stimulus on bone healing. *Clin Orthop Relat R*, 192-198 (2001).

12 Wang, J., Leung, K. S., Chow, S. K. H. & Cheung, W. H. The Effect of Whole Body Vibration on Fracture Healing - a Systematic Review. *Eur Cells Mater* **34**, 108-127, doi:10.22203/eCM.v034a08 (2017).

13 Bao, Q. W. *et al.* An appropriate Wnt/beta-catenin expression level during the remodeling phase is required for improved bone fracture healing in mice. *Sci Rep-Uk* **7**, doi:ARTN 269510.1038/s41598-017-02705-0 (2017).

14 Hegde, V., Jo, J. E., Andreopoulou, P. & Lane, J. M. Effect of osteoporosis medications on fracture healing. *Osteoporosis Int* **27**, 861-871, doi:10.1007/s00198-015-3331-7 (2016).

15 Schindeler, A., McDonald, M. M., Bokko, P. & Little, D. G. Bone remodeling during fracture repair: The cellular picture. *Semin Cell Dev Biol* **19**, 459-466, doi:10.1016/j.semcdb.2008.07.004 (2008).

16 Paul, G. R., Wehrle, E., Tourolle né Betts, D. C., Kuhn, G. & Müller, R. Reducing variance in a mouse defect healing model: Real-time Finite Element Analysis allows homogenization of tissue scale strains *bioRxiv*, doi:10.1101/2020.09.02.274878 (2020).

17 Wehrle, E. *et al.* In vivo micro-CT based approach for discrimination of physiological and impaired healing patterns in mouse femur defect models. . *European Cell and Materials* **31**, 168 (2016).

18 Wehrle, E. *et al.* Evaluation of longitudinal time-lapsed in vivo micro-CT for monitoring fracture healing in mouse femur defect models. *Sci Rep-Uk* **9**, doi:ARTN 1744510.1038/s41598-019-53822-x (2019).

19 Tourolle né Betts D.C., W. E., Pau G.R., Kuhn G.A., Christen P., Hofmann S, Müller R. The association between mineralised tissue formation and the mechanical local in vivo environment: Time-lapsed quantification of a mouse defect healing model. *Sci Rep-Uk* **10**, doi:https://doi.org/10.1038/s41598-020-57461-5 (2020).

20 Li, C. *et al.* Sclerostin Antibody Treatment Enhances Fracture Healing and Increases Bone Mass and Strength in Non-Fractured Bones in an Adult Rat Closed Femoral Fracture Model. *Osteoporosis Int* **22**, 11-12 (2011).

21 Mcdonald, M. M. *et al.* Bone volume is not altered with unloading in the homozygous sclerostin knockout mouse. *Bone* **50**, S94-S94, doi:10.1016/j.bone.2012.02.282 (2012).

598 22 Ominsky, M. S. *et al.* Inhibition of Sclerostin by Monoclonal Antibody Enhances Bone Healing
599 and Improves Bone Density and Strength of Nonfractured Bones. *Journal of Bone and*
600 *Mineral Research* **26**, 1012-1021, doi:10.1002/jbmr.307 (2011).
601 23 Robling, A. G. *et al.* Mechanical stimulation of bone in vivo reduces osteocyte expression of
602 Sost/sclerostin. *J Biol Chem* **283**, 5866-5875, doi:10.1074/jbc.M705092200 (2008).
603 24 Suen, P. K. *et al.* Sclerostin Monoclonal Antibody Enhanced Bone Fracture Healing in an Open
604 Osteotomy Model in Rats. *J Orthop Res* **32**, 997-1005, doi:10.1002/jor.22636 (2014).
605 25 Liu, C. *et al.* Effects of mechanical loading on cortical defect repair using a novel
606 mechanobiological model of bone healing. *Bone* **108**, 145-155,
607 doi:10.1016/j.bone.2017.12.027 (2018).
608 26 Gupta, R. R. *et al.* Axial strain enhances osteotomy repair with a concomitant increase in
609 connexin43 expression. *Bone Res* **3**, doi:ARTN 1500710.1038/boneres.2015.7 (2015).
610 27 Schwarz, C. *et al.* Mechanical Load Modulates the Stimulatory Effect of BMP2 in a Rat
611 Nonunion Model. *Tissue Eng Pt A* **19**, 247-254, doi:10.1089/ten.tea.2012.0265 (2013).
612 28 Tufekci, P. *et al.* Early mechanical stimulation only permits timely bone healing in sheep. *J*
613 *Orthop Res* **36**, 1790-1796, doi:10.1002/jor.23812 (2018).
614 29 Leung, K. S. *et al.* Low-Magnitude High-Frequency Vibration Accelerates Callus Formation,
615 Mineralization, and Fracture Healing in Rats. *J Orthop Res* **27**, 458-465,
616 doi:10.1002/jor.20753 (2009).
617 30 van Oers, R. F. M., Wang, H. & Bacabac, R. G. Osteocyte Shape and Mechanical Loading. *Curr*
618 *Osteoporos Rep* **13**, 61-66, doi:10.1007/s11914-015-0256-1 (2015).
619 31 Vatsa, A. *et al.* Osteocyte morphology in fibula and calvaria - Is there a role for
620 mechanosensing? *Bone* **43**, 452-458, doi:10.1016/j.bone.2008.01.030 (2008).
621 32 Wu, V. *et al.* Osteocyte morphology and orientation in relation to strain in the jaw bone. *Int J*
622 *Oral Sci* **10**, doi:Unsp 210.1038/S41368-017-0007-5 (2018).
623 33 McKenzie, J. A., Bixby, E. C. & Silva, M. J. Differential Gene Expression from Microarray
624 Analysis Distinguishes Woven and Lamellar Bone Formation in the Rat Ulna following
625 Mechanical Loading. *Plos One* **6**, doi:ARTN e2932810.1371/journal.pone.0029328 (2011).
626 34 Wasserman, E. *et al.* Differential load-regulated global gene expression in mouse trabecular
627 osteocytes. *Bone* **53**, 14-23, doi:10.1016/j.bone.2012.11.017 (2013).
628 35 Zaman, G. *et al.* Loading-related regulation of gene expression in bone in the contexts of
629 estrogen deficiency, lack of estrogen receptor alpha and disuse. *Bone* **46**, 628-642,
630 doi:10.1016/j.bone.2009.10.021 (2010).
631 36 Lara-Castillo, N. *et al.* In vivo mechanical loading rapidly activates beta-catenin signaling in
632 osteocytes through a prostaglandin mediated mechanism. *Bone* **76**, 58-66,
633 doi:10.1016/j.bone.2015.03.019 (2015).
634 37 Melville, K. M. *et al.* Effects of Deletion of ER in Osteoblast-Lineage Cells on Bone Mass and
635 Adaptation to Mechanical Loading Differ in Female and Male Mice. *Journal of Bone and*
636 *Mineral Research* **30**, 1468-1480, doi:10.1002/jbmr.2488 (2015).
637 38 Robling, A. G. *et al.* Sost, independent of the non-coding enhancer ECR5, is required for bone
638 mechanoadaptation. *Bone* **92**, 180-188, doi:10.1016/j.bone.2016.09.001 (2016).
639 39 Moura, M. L. A. *et al.* Estrogen therapy associated with mechanical vibration improves bone
640 microarchitecture and density in osteopenic female mice. *J Anat* **233**, 715-723,
641 doi:10.1111/joa.12893 (2018).
642 40 Paul, G. R., Schwilch, P., Wehrle, E., Kuhn, G. A. & Müller, R. Development of a micro-CT
643 mouse holder for a femur defect mouse model. *bioRxiv*, doi:doi:
644 https://doi.org/10.1101/2020.09.10.289553 (2020).

645
646

647 **Figure Legends**

648 **Figure 1.** Loading system for femur defects in mice. a. Loading fixator (RISystem, Davos,
649 Switzerland) consisting of four PEEK parts connected via two transverse Titanium pins. b.
650 Insertion of loading fixator into loading device with clamping of loading adapter (1) and
651 removal of transverse pin (2). c. Loading device consisting of mouse holder with anaesthesia
652 inlet (1), heated ground plate (2), clamp for fixator (3) and actuation system with loading
653 chuck (4), load cell electronics box (5), electro-magnetic actuator (6), actuator control
654 electronic box (7). The mouse holder can be used for the loading device and the CT scanner
655 without the need to change the position of the mouse. For detailed description and
656 drawings see Paul et al. [40].

657

658 **Figure 2.** Representative images (full image and cut; threshold: 645 mg HA/cm^3) of the
659 defect region from animals of the loading group (week 0-7) and the control group (week 0-
660 7). Visualization of bone formation (orange) and resorption (blue) via registration of micro-
661 CT scans from weeks 1-6 to weeks 0-5.

662

663 **Figure 3**. Micro-CT based evaluation of bone parameters in the loading group (red) and the
664 control group (blue) using different VOIS (pre-loading healing period highlighted in lighter
665 color; loading period highlighted in darker color): defect center (DC; a-c), defect periphery
666 (DP; d-f), cortical fragment center (FC; g-i), cortical fragment periphery (FP; j-l). a, d, g, j:
667 Bone formation rate (solid line) and bone resorption rate (dashed line) given in percent per
668 day. b, e, h, k: Bone volume (BV) normalized to TV (DC for DC and DP, FC for FC+FP). c, f, i, l:
669 Degree of bone mineralization given as ratio of bone volume with a density ≥645 mg HA/cm^3
670 to the total osseous volume (threshold ≥395 mg HA/cm^3). n=10 per group; * indicates p <

671 0.05 determined by two-way ANOVA with Geisser-Greenhouse correction and Bonferroni
672 correction.
673
674 **Figure 4.** Micro-CT and histological analyses of consecutive callus sections. a, b: Micro-CT
675 images of fracture callus sections corresponding to sections stained with Safranin-O for one
676 animal from the loading (a) and the control group (b): CT image (threshold: 395 mg HA/cm^3),
677 visualization of regions of bone formation and resorption via registration of CT image from
678 weeks 6 and 7, visualization of strains on CT section via micro-FE analysis for week 7 and
679 week 6. c-j. Consecutive longitudinal sections of fractured femora 7 weeks after defect
680 surgery of one animal from the loading group and the control group stained for Safranin-O
681 (c-f), Sclerostin (g, h), Rankl (i, j). Scale bar = 100 µm (c, d), scale bar = 500 µm (e-j).
682
683 **Figure 5.** Visualization of local cellular distribution patterns and protein expression in the
684 fracture callus and adjacent cortex. a. Longitudinal Safranin-O stained sections of fractured
685 femora 7 weeks after defect surgery of one animal from the loading group and one animal
686 from the control group. Boxes indicate regions depicted in b (1: callus; 2: cortex); Scale bar =
687 100 µm. b. Magnification of callus region (left) and cortical region (right) stained for
688 Safranin-O, Sclerostin and Rankl; Scale bar = 50 µm.
689
690
691
692
693

Tables

Table 1. Fracture healing outcome assessed by cortical bridging (healed fracture ≥ 3 bridged cortices, threshold 395 mg HA/cm^3).

		week							
	Group (n=10)	0	1	2	3	4	5	6	7
Healed fractures per group	Control/Loading	0/0	0/0	5/6	9/10	10/10	10/10	10/10	10/10

Figure 1

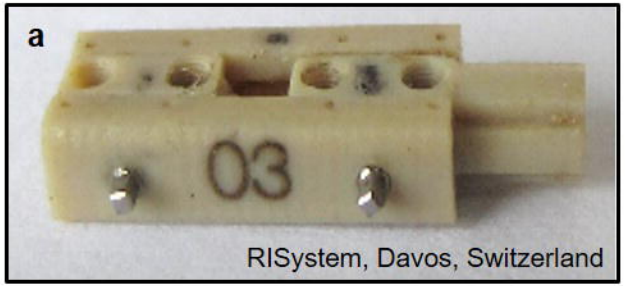
a
03
RISystem, Davos, Switzerland

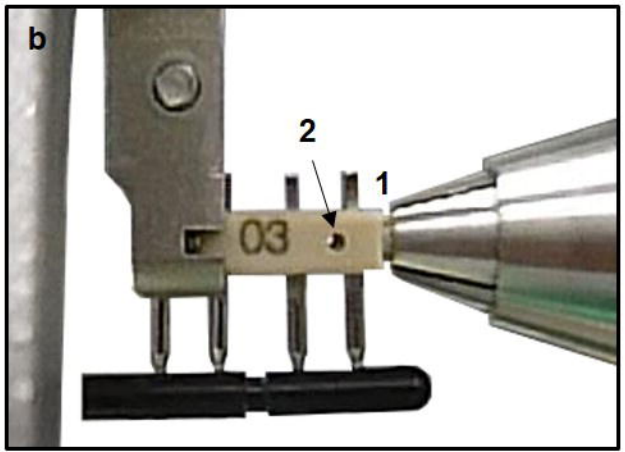
b
2
1
03

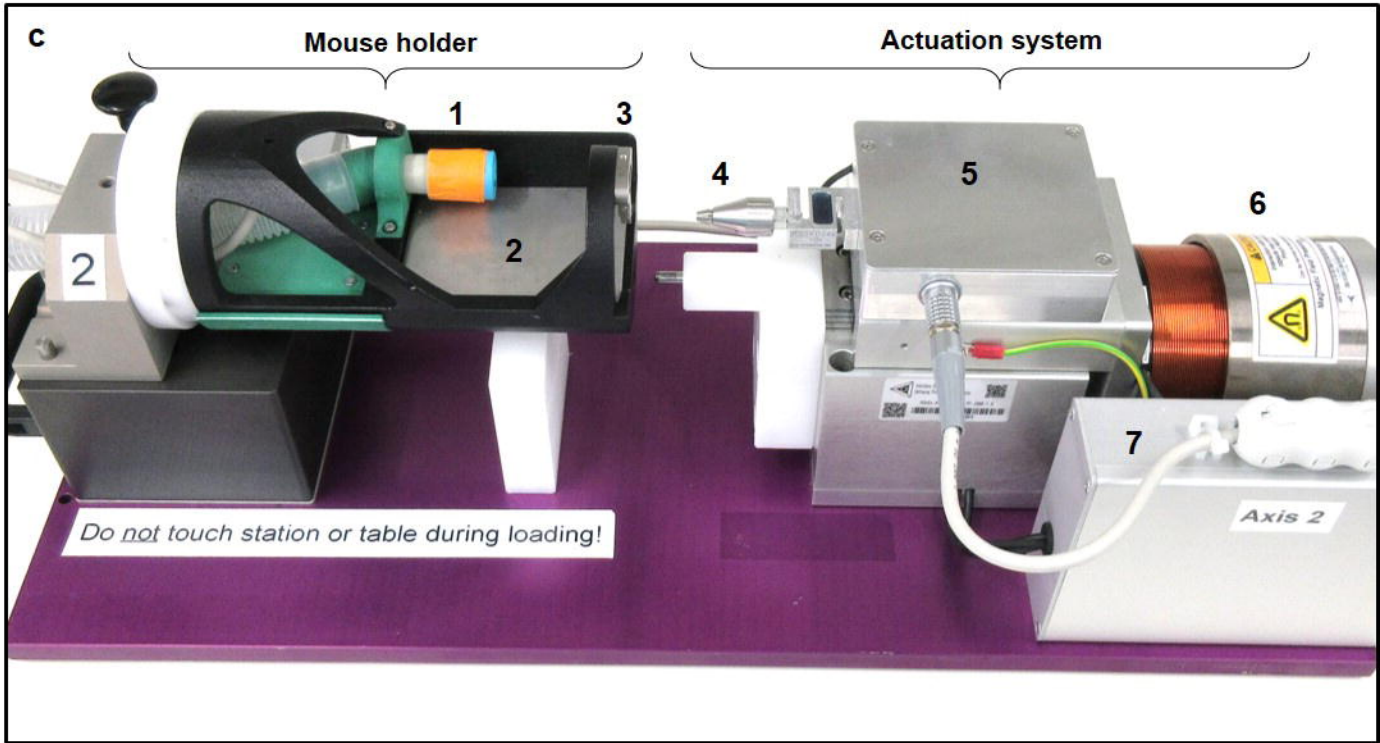
c
Mouse holder
Actuation system
1
3
4
5
6
2
2
7
Do not touch station or table during loading!
Axis 2

Figure 2

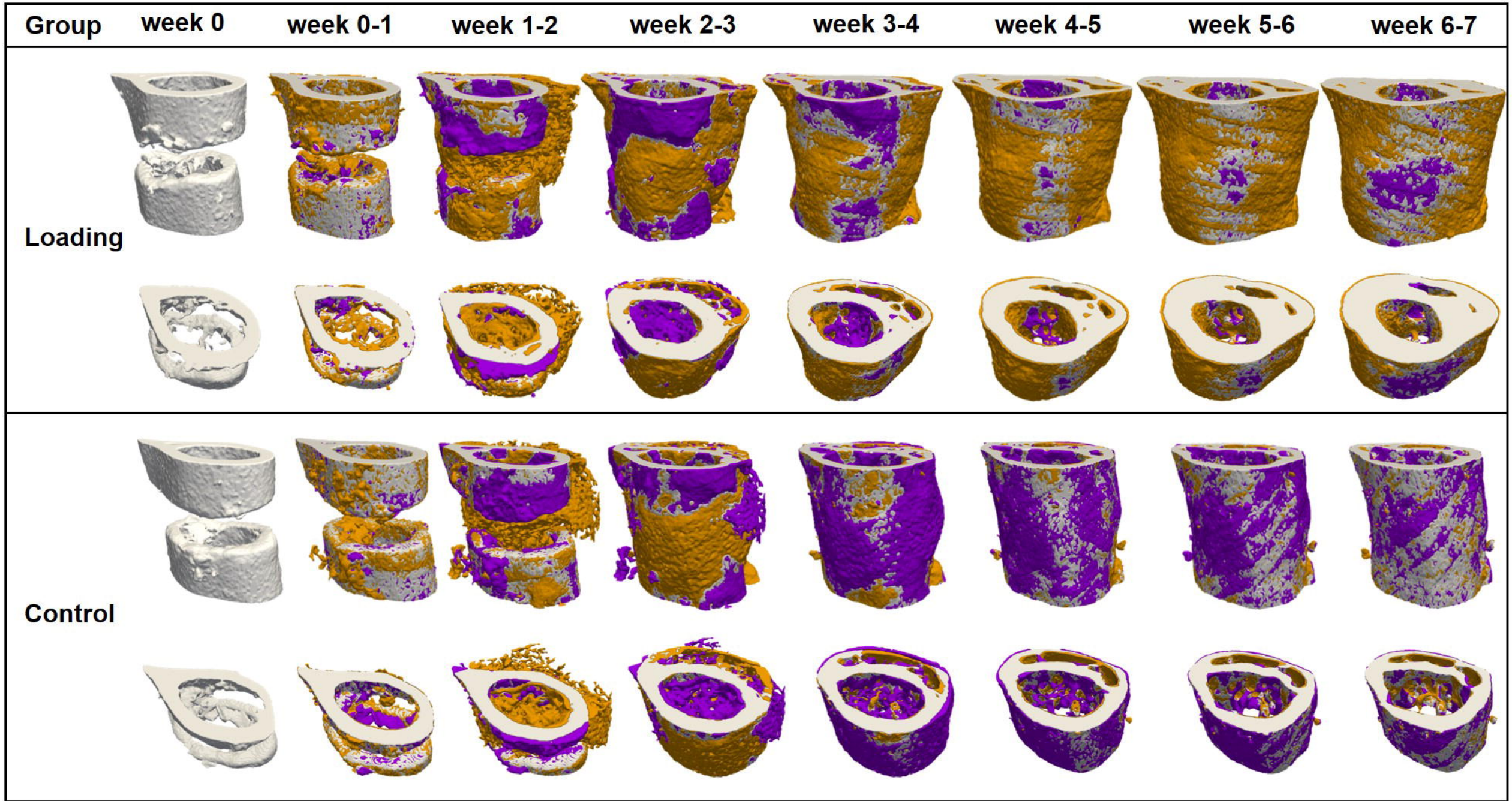
Group
week 0
week 0-1
week 1-2
week 2-3
week 3-4
week 4-5
week 5-6
week 6-7
Loading
Control

Figure 3

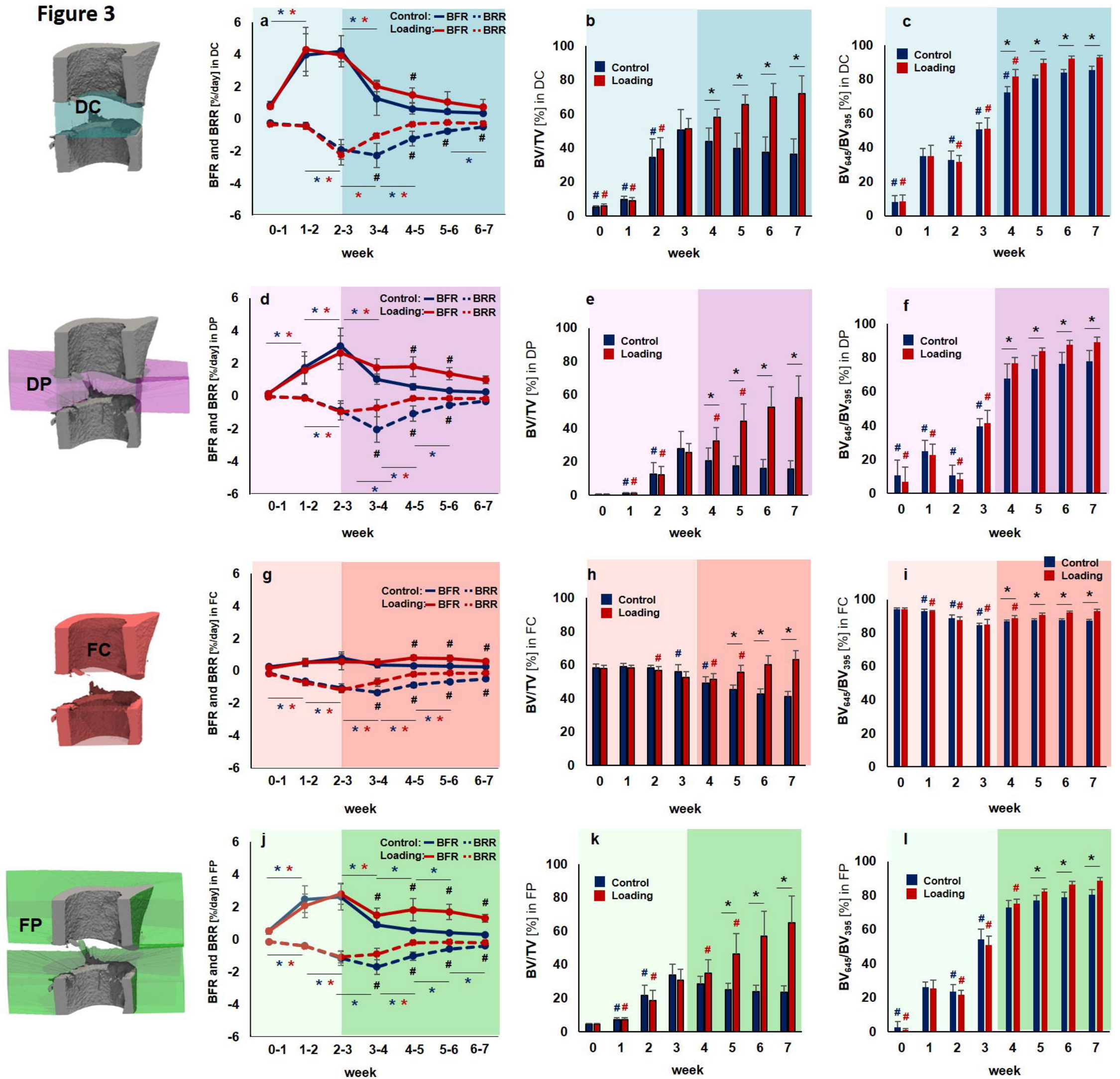
DC
DP
FC
FP
a
b
c
d
e
f
g
h
i
j
k
l
Control: BFR BRR
Loading: BFR BRR
Control
Loading
BFR and BRR [%/day] in DC
BV/TV [%] in DC
BV645/BV395 [%] in DC
BFR and BRR [%/day] in DP
BV/TV [%] in DP
BV645/BV395 [%] in DP
BFR and BRR [%/day] in FC
BV/TV [%] in FC
BV645/BV395 [%] in FC
BFR and BRR [%/day] in FP
BV/TV [%] in FP
BV645/BV395 [%] in FP
0-1 1-2 2-3 3-4 4-5 5-6 6-7
0 1 2 3 4 5 6 7
week

Figure 4

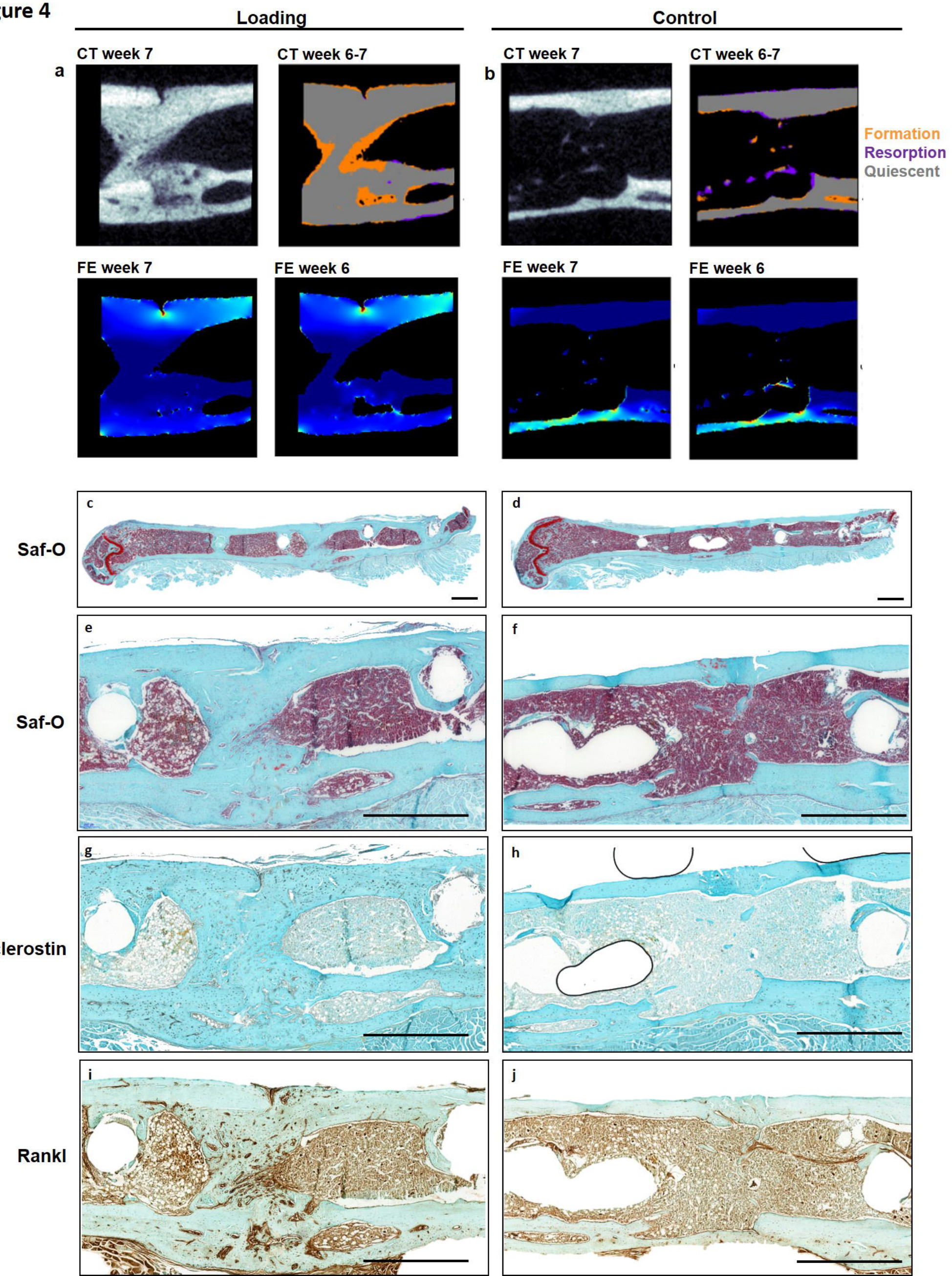
Loading
Control
a
CT week 7
CT week 6-7
b
CT week 7
CT week 6-7
Formation
Resorption
Quiescent
FE week 7
FE week 6
FE week 7
FE week 6
c
d
Saf-O
e
f
Saf-O
g
h
Sclerostin
i
j
Rankl

Figure 5

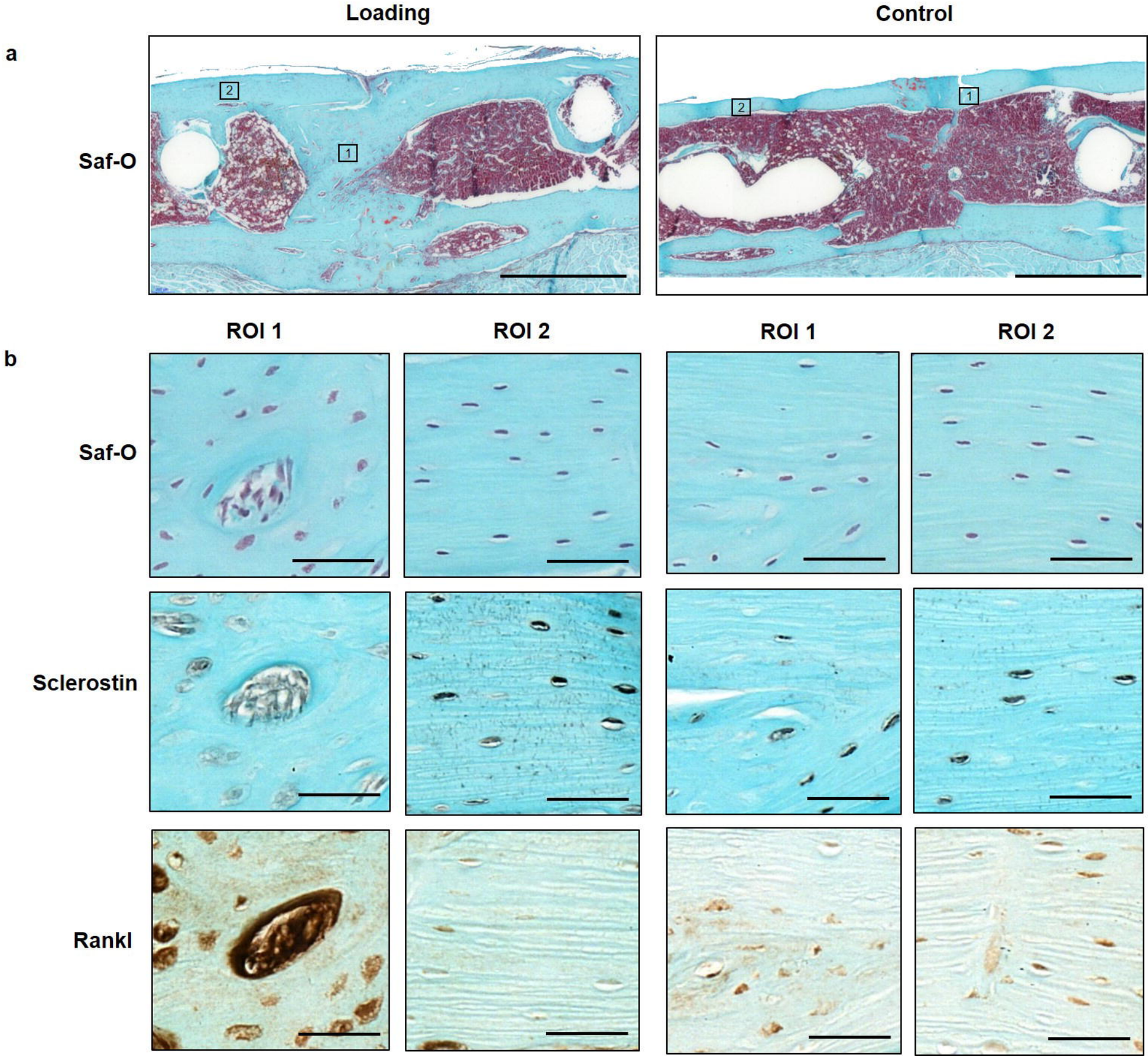
Loading
Control
a
Saf-O
2
1
2
1
b
ROI 1
ROI 2
ROI 1
ROI 2
Saf-O
Sclerostin
Rankl